Carbon 202 (2023) 204–212

Contents lists available at ScienceDirect

Carbon

journal homepage: www.elsevier.com/locate/carbon

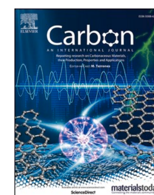

In-situ monitoring of microwave plasma-enhanced chemical vapour deposition diamond growth on silicon using spectroscopic ellipsometry

William G.S. Leigh [a,b,*], Evan L.H. Thomas [a], Jerome A. Cuenca [a], Soumen Mandal [a], Oliver A. Williams [a]

[a] *School of Physics and Astronomy, Cardiff University, Cardiff, UK*
[b] *EPSRC Centre for Diamond Science and Technology, UK*

A R T I C L E I N F O

Keywords:
CVD Diamond
In-situ monitoring
Spectroscopic ellipsometry
Diamond films
Characterisation

A B S T R A C T

The quality of polycrystalline diamond films is heavily dependent on the nucleation and early stages of growth, making the ability to monitor these early stages highly desirable. Spectroscopic ellipsometry (SE) allows for real-time monitoring of the thickness, composition, and morphology of films with sub-nanometre precision. In this work, *ex-situ* SE spectra were used to develop an optical model for film characterisation, which was then applied to *in-situ* data. The coalescence of individual crystallites into a single film was observed through a parabolic decrease in void content followed by peaks in sp^2 content and surface roughness. These observations were validated using *ex-situ* Raman spectra and AFM images of samples grown for durations between 5 and 30 min. The model was also used to investigate the impact of varying the methane concentration, finding that a higher methane fraction resulted in earlier coalescence and a higher peak in sp^2 content. This work demonstrates that SE is a powerful tool for monitoring and optimisation of the critical early stages of polycrystalline diamond growth.

1. Introduction

Polycrystalline diamond films exhibit many of the extreme properties of bulk diamond, allowing for exploitation of these properties over large areas at a significantly lower cost [1]. This presents applications such as microelectromechanical systems [2], boron-doped diamond electrodes [3] and thermal management solutions [4,5]. However, the quality of these films is very dependent on the seeding and early stages of growth [6]. Additionally, a significant limiting factor for the use of diamond as a thermal management solution is the thermal barrier at the substrate-diamond interface, associated with the disordered transition region [7]. Therefore, the ability to monitor these early stages of growth is incredibly important to optimise growth conditions.

The harsh plasma environment during microwave plasma-enhanced chemical vapour deposition (MPECVD) diamond growth largely limits *in-situ* monitoring to optical techniques [8], with the relatively high pressure during growth precluding the use of electron-based techniques such as reflection high-energy electron diffraction. Pyrometric and laser interferometry [9–11] are commonly used for the monitoring of film thickness, but do not provide any compositional information. Whilst Raman spectroscopy is also commonly used for characterisation of diamond films [12], it is significantly more sensitive to non-diamond carbon and completely insensitive to void [13]. Spectroscopic ellipsometry (SE) provides advantages over existing optical techniques, demonstrating an ability to determine the thickness and diamond, sp^2 and void fractions (with close to equal sensitivity) of films as thin as 4 nm [14]. SE involves the measurement of changes in polarisation state of light upon reflection from a sample. Measured spectra are compared to those simulated by an optical model of the sample structure, with an iterative fitting process used to improve the model to minimise the mean square error (MSE) between the two [15]. As the measurement is of the change in polarisation state and not intensity of the reflected light, the measurement is possible even when there is a bright background [16].

Due to a number of factors, including the large free surface energy difference between diamond (6 J m^{-2}) and silicon (1.5 J m^{-2} for {100}) [17], the low sticking coefficient of gaseous precursors and the lattice parameter mismatch, the nucleation density of diamond on untreated silicon is on the order of 10^4-10^5 cm^{-2}, which is too low for the growth of coalesced films [1,18–20]. A pre-treatment step, such as electrostatically seeding the wafer with diamond nanoparticles [21] or mechanical

Abbreviations: CVD, Chemical Vapour Deposition.

* Corresponding author. School of Physics and Astronomy, Cardiff University, Cardiff, UK.
E-mail address: leighwg@cardiff.ac.uk (W.G.S. Leigh).

https://doi.org/10.1016/j.carbon.2022.10.049
Received 6 September 2022; Received in revised form 18 October 2022; Accepted 20 October 2022
Available online 25 October 2022
0008-6223/© 2022 The Authors. Published by Elsevier Ltd. This is an open access article under the CC BY license (http://creativecommons.org/licenses/by/4.0/).

abrasion with diamond grit [22] is necessary to enhance nucleation. Diamond growth on silicon will generally follow the Volmer-Weber growth mechanism, with adatoms preferentially bonding to existing nuclei, resulting in the formation of isolated islands [17]. These islands expand both laterally and vertically until they coalesce, with the intersection of crystallites causing the trapping of non-diamond carbon within grain boundaries [23]. At this point, growth proceeds via the columnar van-der Drift model, with competitive overgrowth of crystallites resulting in increased surface roughness and crystallite size with increasing thickness [24,25].

Previous attempts at SE characterisation of diamond films have employed a Bruggeman effective medium approximation to mix reference optical constants of the various components of the film, modelling it as a single bulk layer [8,26–28]. Reductions in MSE were achieved by the inclusion of components to approximate sp^2 and void content, as well as the addition of a layer to account for surface roughness [8,13,28]. Lateral Volmer-Weber growth of islands is observed as a parabolic reduction in void content, with a sharp peak in sp^2 content resulting from the trapping of non-diamond content within grain boundaries [8,14,28]. The majority of previous SE characterisation of diamond films was carried out on substrates pretreated using mechanical abrasion [8]. Due to the damage to the silicon substrate caused by this technique, a rough amorphous silicon layer was observed on the surface of the substrate. The similarity between the optical constants of this layer and the diamond film components prevented the detection of diamond in the very early stages of growth, necessitating the fixing of bulk volume fractions for this period [8]. Recently, an SE study of substrates seeded with diamond nanoparticles has removed this limitation, as this seeding technique does not cause substrate damage [28].

In this work, application of SE to the early stages of polycrystalline diamond growth on silicon is demonstrated. *Ex-situ* spectra are used to build up an optical model for film characterisation which is then applied to *in-situ* spectra, taken in the first 30 min of growth. This model is validated using *ex-situ* atomic force microscopy (AFM) and Raman spectroscopy. The model is later used to investigate the impact of different methane concentrations during growth.

2. Material and methods

All samples were grown on 15 × 15 mm, 0.5 mm thick polished P-type Si {100} wafers. Prior to seeding, all wafers were cleaned using the RCA SC-1 process [29,30] to remove any organic residues and ensure a uniform native oxide thickness. Silicon substrates require pre-treatment to result in sufficient nucleation densities for the growth of coalesced diamond films [1,18]. This was done by immersing substrates in a hydrogen-terminated/DI H_2O colloid for 10 min. The seeding technique used is known to result in seeding densities in excess of 10^{11} cm^{-1} [21].

Growth was carried out in a Carat Systems CTS6U clamshell-type microwave CVD reactor, at a microwave power of 3 kW and a chamber pressure of 55 Torr. Substrate temperatures were measured at approximately 710 °C using a WilliamsonIR Pro92 dual-wavelength pyrometer. This relatively low substrate temperature was chosen to result in a slower growth rate and therefore greater resolution for the *in-situ* SE monitoring. 5 samples were grown for durations of 5–30 min at 3% methane diluted in hydrogen. 2 further growths were carried out to investigate the effect of a variance in methane flow rate, one for 30 min at 5% methane, the other for 90 min at 1% methane. The plasma was sparked at a microwave power of 1.5 kW and chamber pressure of 15 Torr, with microwave power and chamber pressure ramped up to growth conditions over a period of 3 min. This ramp up in power and pressure was software-controlled to ensure that the process was uniform for all samples. The growth timer was started at the conclusion of this ramp as soon as the microwave power and chamber pressure reached growth conditions. Methane concentration remained constant throughout the spark, ramp up and growth process. At the end of each growth, samples were cooled in a purely hydrogen-fed plasma to reduce the formation of non-sp^3 material.

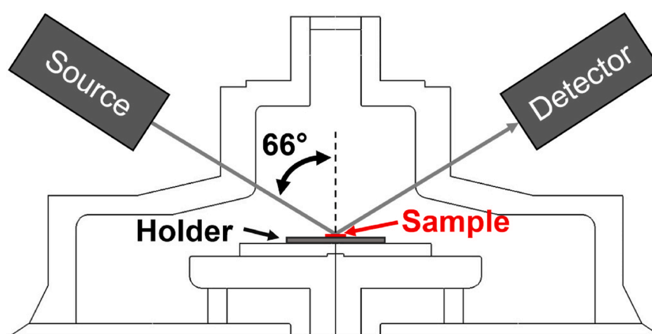

Fig. 1. Schematic of the reactor showing the measurement of in-situ SE spectra. The thickness of the sample is exaggerated for visibility. (A colour version of this figure can be viewed online.)

Spectroscopic ellipsometry was performed both *in-situ* and *ex-situ* with a J. A. Woollam M-2000D rotating compensator ellipsometer and CompleteEASE software over a wavelength range of 300–1000 nm. *In-situ* acquisitions were taken through fixed fused silica viewports, at an angle of incidence of approximately 66°, with an acquisition time of 1s. Fig. 1 shows a schematic of the setup used for collection of *in-situ* SE spectra. *Ex-situ* spectra were taken at incidence angles of 65, 70 and 75°. An iterative fitting process (detailed in section 3.1) was used, with various sample structures iterated within the CompleteEASE software to minimise the difference between simulated and measured spectra.

Raman spectroscopy was performed using a HORIBA LabRAM spectrometer using an excitation wavelength of 473 nm, chosen to maximise sensitivity to both sp^2 and sp^3 carbon [31]. Atomic force microscopy was carried out using a Bruker Dimension Icon microscope in peak force tapping mode with a ScanAsyst tip.

3. Results and discussion

3.1. Ex-situ SE

Ex-situ spectra of the 20-min growth duration sample were used to develop an optical model for characterisation of other samples, with an iterative fitting process used to minimise the mean square error (MSE) between simulated and measured spectra. Fig. 2 shows the development of this model throughout the fitting process.

The initial model consisted of a bulk layer comprising two oscillators matched to optical constants of type I and II natural diamond [32] atop a silicon substrate [33]. This resulted in an MSE of over 100, so was unsuitable for characterisation of the sample. Addition of a layer to account for surface roughness, a Bruggeman EMA made up of 50% bulk layer and 50% void, resulted in a huge reduction in MSE to 25.72. A further reduction in MSE by almost 50% to 13.66 was achieved by changing the bulk layer to a second EMA, mixing optical constants of diamond and void, with the bulk void fraction allowed to vary. The optical constants of glassy carbon [34] have previously been shown to be a good approximation for sp^2 content in the bulk layer [28]. Addition of this third component to the bulk EMA reduced MSE again to 10.18.

Prior to seeding, a 1.69 nm-thick native oxide layer was observed on the surface of the silicon substrates by SE. However, addition of this to the optical model of the 20-min sample increased the MSE, so this was not included in future iterations. It is worth noting that H_2 and H_2/CH_4 plasmas have been shown to result in etching of the native oxide of silicon [35,36]. Previous XPS and SE studies have also identified the existence of a sub-10 nm amorphous SiC layer in the early stages of diamond growth, resulting from carburisation of the silicon substrate [28,37,38]. A final reduction in MSE to 6.09 was achieved by the inclusion of an interfacial 7.38 nm layer of cubic SiC [32] between the substrate and bulk layer. When applied to samples with a growth

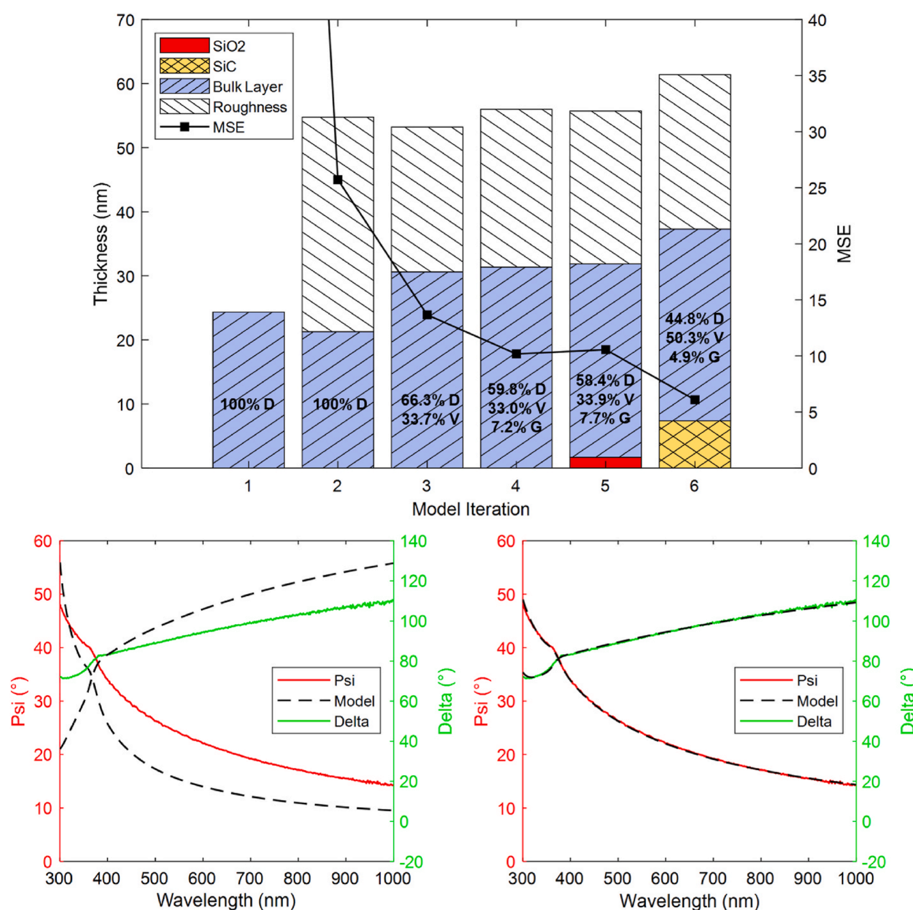

Fig. 2. Above: Development of the model fitted to the 20-min growth duration sample, showing MSE, layer thicknesses, and bulk layer diamond (D), void (V) and glassy carbon (G) content for each iteration of the model. Below: Comparison of the modelled parameters with measured parameters at an incidence angle of 70° for the first iteration (left) and final iteration (right). (A colour version of this figure can be viewed online.)

duration of 15 min or less, removal of the surface roughness layer did not significantly impact MSE, so was unnecessary to include when characterising these samples.

3.2. *In-situ* SE

The application of the model to *in-situ* data required several additional considerations. The in-plane window effects were accounted for using spectra of a reference sample as detailed in Ref. [39]. At CVD diamond growth conditions, substrate temperatures routinely exceed 700 °C [8,40,41], influencing the optical properties of the silicon substrate. As the refractive index of nanocrystalline diamond films does not vary substantially with temperature [42], it was unnecessary to vary the optical constants of the film components. The SiC layer optical constants were similarly not varied as the trajectories of ellipsometric parameters are very close together for extremely thin films [43]. The substrate temperature at growth conditions was extracted using a library of temperature-dependent optical constants of silicon within the CompleteEASE software, built by interpolating optical constants at known temperatures using an algorithm based on the critical point shifting algorithm detailed in Ref. [44]. Whilst this method of determining the temperature proved effective in the initial stages, a high degree of parameter correlation between temperature and bulk layer glassy carbon fraction was observed as the film approached coalescence. As a result of this, the temperature was fixed at a point 1 min after the completion of the ramp up to growth conditions. As with the *ex-situ* spectra, addition of a roughness layer to the model proved unnecessary in the initial stages but was required later. A roughness layer was

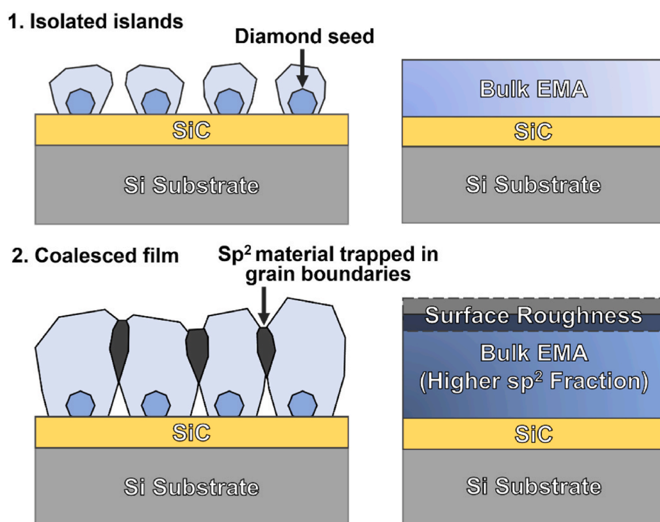

Fig. 3. Schematic of the growth process (left), with the optical models used to fit each stage (right). (A colour version of this figure can be viewed online.)

included in the model from 18 min, the point at which its inclusion reduced the MSE by more than 10%. This is consistent with the *ex-situ* characterisation, with a roughness layer not necessary in the 15-min growth duration sample but needed in the 20-min growth duration sample. A schematic of sample morphology and the optical models used

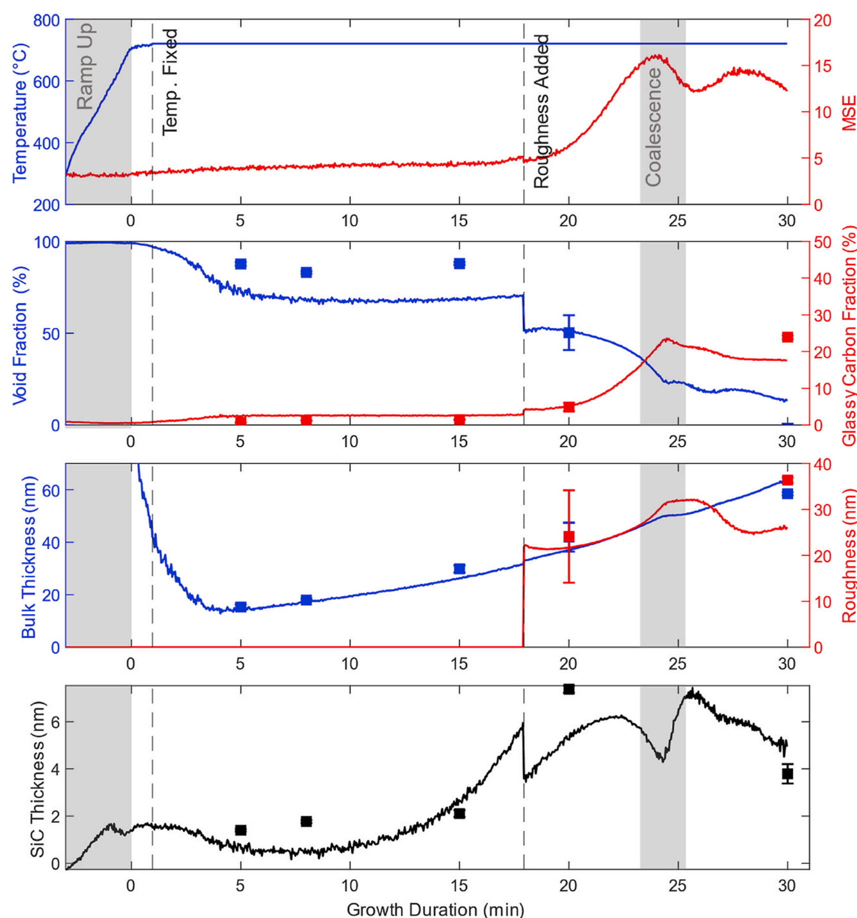

Fig. 4. *In-situ* SE-measured data from a 30-min growth at 3% methane concentration. From top panel: SE-measured temperature and MSE; bulk layer impurity fractions; bulk thickness and surface roughness; SiC layer thickness. The square points plotted are from *ex-situ* spectra of samples of the same growth duration. (A colour version of this figure can be viewed online.)

to fit SE data can be seen in Fig. 3, showing the increase in surface roughness and sp^2 content upon coalescence.

Fig. 4 shows data from the *in-situ* SE model for a sample of growth duration 30 min with 3% methane concentration. In the first 4 min of growth, a high level of parameter correlation is present. Parameter correlation is the result of the data fitting process where the sensitivity of multiple parameters (in this case bulk layer thickness and void content) exhibits the same spectral signature, meaning that the parameter values determined are not unique; there are multiple combinations of bulk thickness and void content values that produce the same quality of fit [45]. In this case, the fitting process suggests a modelled structure with an unrealistically thick bulk layer with very high void content. After 4 min, this correlation had decreased and resulted in a more realistic model. This does illustrate the importance of validation of the SE model using alternative measurement techniques. From approximately 18 min of growth, a parabolic decrease in the bulk void fraction is seen as the individual islands expand laterally. Just before 25 min, a peak in glassy carbon content of approximately 23.5% is seen, due to the trapping of non-diamond carbon in grain boundaries following the coalescence of the individual crystallites into single film. The parabolic decrease in bulk void content followed by a peak in sp^2 content at the point of coalescence is consistent with what has been previously seen [8,14,28]. If the individual islands are assumed to be hemispheres arranged on a hexagonal grid, contact between them would occur at a void fraction of 40%. However, in reality the islands are not as efficiently spaced or perfectly hemispherical. As a result, the contact between islands, marked by the beginning of a steep decrease in void fraction and corresponding increase in sp^2 content, occurs at approximately 50% void fraction. This is closer to the contact at 48% void fraction predicted by modelling the islands as hemispheres on a square grid, a less efficient spacing [14].

The SiC layer increased in thickness up to the point of coalescence, before starting to decrease in thickness following coalescence. This trend matches previous SE analysis of early-stage diamond growth on silicon seeded with diamond nanoparticles [28].

When comparing *in-situ* and *ex-situ* data, it can be seen that prior to coalescence, the *ex-situ* model suggests a higher void fraction and lower glassy carbon fraction. It is likely that this is at least partially the result of the process of cooling in a hydrogen plasma, which is known to preferentially etch non-diamond carbon [46]. Immediately before and after coalescence, the reduction in glassy carbon fraction is not seen. The process of coalescence results in the trapping of sp^2 material in the grain boundaries, and as a result it is inaccessible to the plasma, reducing the etching possible.

A peak in the roughness layer was also seen around the point of coalescence, as the crystallites reach a maximum size prior to forming a coalesced film. This roughness decreased after coalescence, before again increasing due to the overgrowth of competing crystallites [47].

The *ex-situ* SE data displayed the same trends in bulk impurity content, bulk thickness and SiC thickness, although the exact values of the bulk impurity fractions differ slightly. Prior to coalescence, *ex-situ* data suggests a lower sp^2 bulk fraction as well as a greater void fraction than is seen in the *in-situ* data. This may be in part due to the cooling of samples in a purely hydrogen fed plasma, which is known to etch sp^2 carbon at a much faster rate than sp^3 material [37].

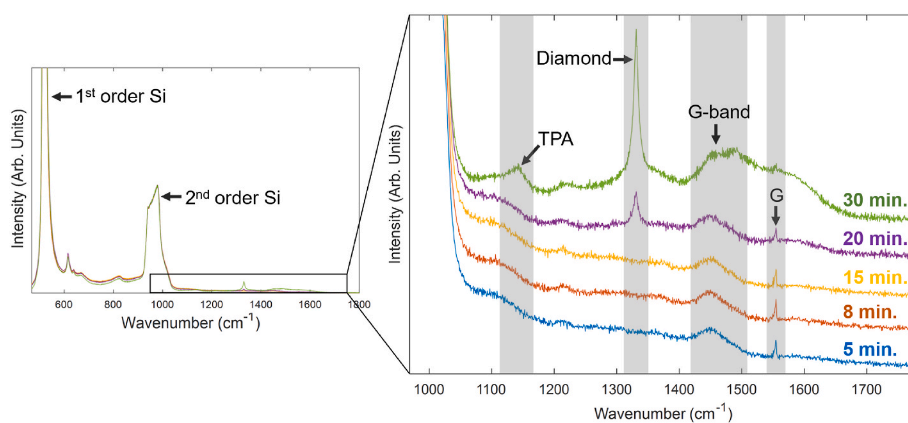

Fig. 5. Left: *Ex-situ* Raman spectra of samples of varying growth duration, normalised to the second-order silicon Raman peak. Right: Magnified view of the same spectra, offset for clarity. (A colour version of this figure can be viewed online.)

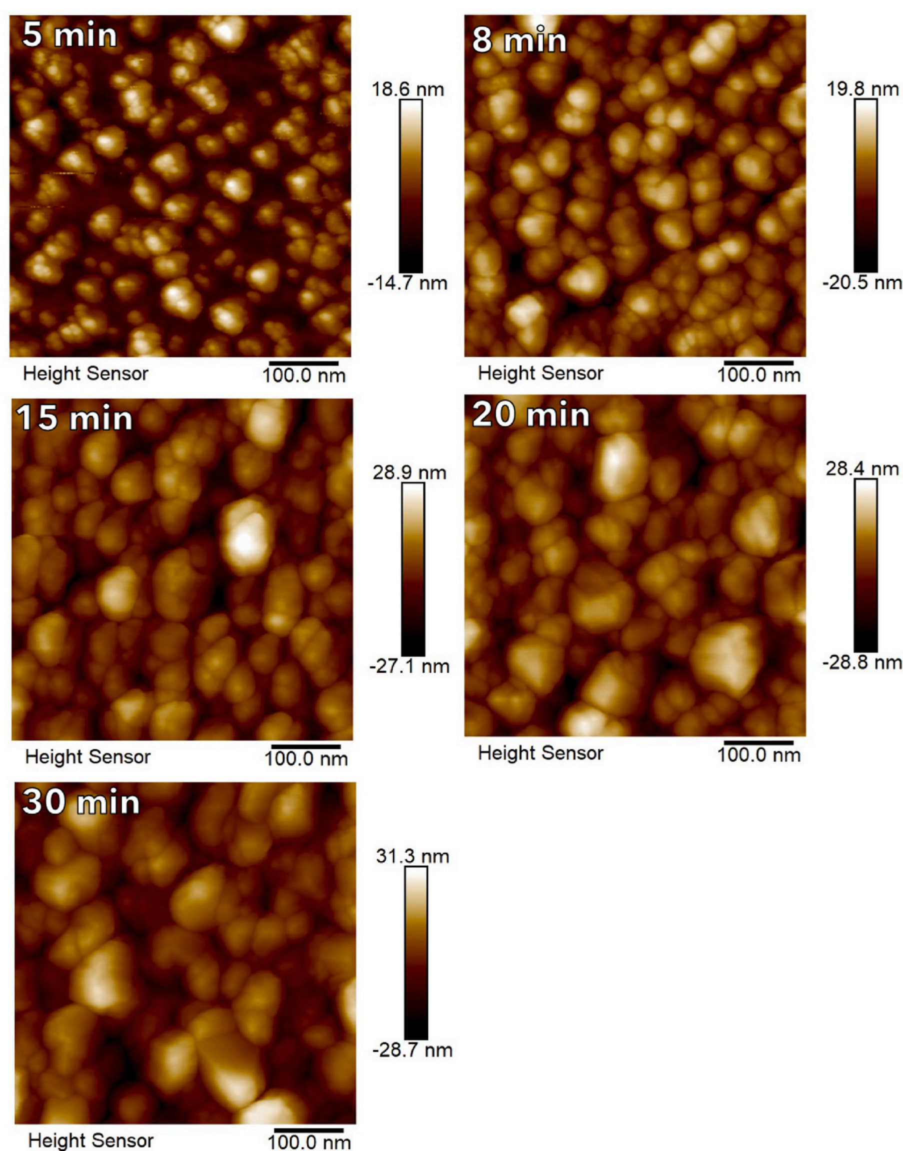

Fig. 6. AFM images of samples grown for durations of 5–30 min. (A colour version of this figure can be viewed online.)

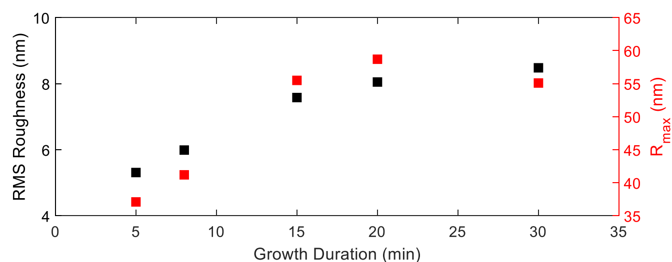

Fig. 7. RMS roughness and maximum roughness depth for samples of varying growth duration. (A colour version of this figure can be viewed online.)

3.3. Raman spectroscopy

Fig. 5 shows *ex-situ* Raman spectra of several samples with growth duration from 5 to 30 min, normalised to the second order silicon Raman peak at 950 cm^{-1}. As is to be expected for such early stage diamond growth, the most significant peaks in the spectrum are from the silicon substrate; the first and second-order Raman peaks at 520 and 980 cm^{-1} [48], with the minor peak at approximately 830 cm^{-1} also part of the second-order silicon spectrum [49,50]. The two peaks at 620 and 644 cm^{-1} are the result of local vibrational modes of boron atoms within the doped substrate [51,52].

In the magnified spectra, which are offset for clarity, the first-order diamond Raman peak at 1332.5 cm $^{-1}$ is only visible from 20 min onwards. This corresponds with the SE model, which indicates an increase in bulk diamond content from approximately 18 min onwards. By 30 min, the diamond Raman peak has significantly increased, consistent with the SE model showing coalescence just before 25 min, with the corresponding increase in bulk layer diamond content at this point. As is typical for nanocrystalline films, the first-order diamond Raman peak exhibits broadening due to the limited thickness and crystallite size [53,54].

In-plane stretching of pairs of sp^2 sites results in the G-band, which is seen here at approximately 1450 cm^{-1}. Whilst typically seen closer to 1560 cm^{-1} [53], a downshift in the position of this peak indicates an increased level of disorder with the sp^2 material, suggesting that is more amorphous in nature [53]. This band is more intense in the 30-min growth duration sample. The G peak, caused by bond stretching of pairs of sp^2 atoms in both rings and chains [55], is visible in all samples at 1555 cm^{-1}, although it is obscured by the G-band in the 30-min sample.

Only visible in the 30-min growth duration sample is a peak at 1140 cm^{-1}, assigned to *trans*-polyacetylene, present within the grain boundaries [12]. The lack of this peak in the 20-min sample suggests coalescence (and therefore formation of grain boundaries) occurs between 20 and 30 min, again consistent with the SE model's prediction of it occurring immediately prior to 25 min. Whilst this peak is always accompanied by a second peak at 1450 cm^{-1} [12], the 1450 cm^{-1} peak is obscured by the G-band.

3.4. Atomic force microscopy

Fig. 6 shows AFM images of samples grown for varying duration, whilst Fig. 7 shows the RMS roughness and maximum roughness depth (R_{max}) of the same samples. In the 5-min growth duration sample, individual islands are visible. The lateral sizes of these islands increase

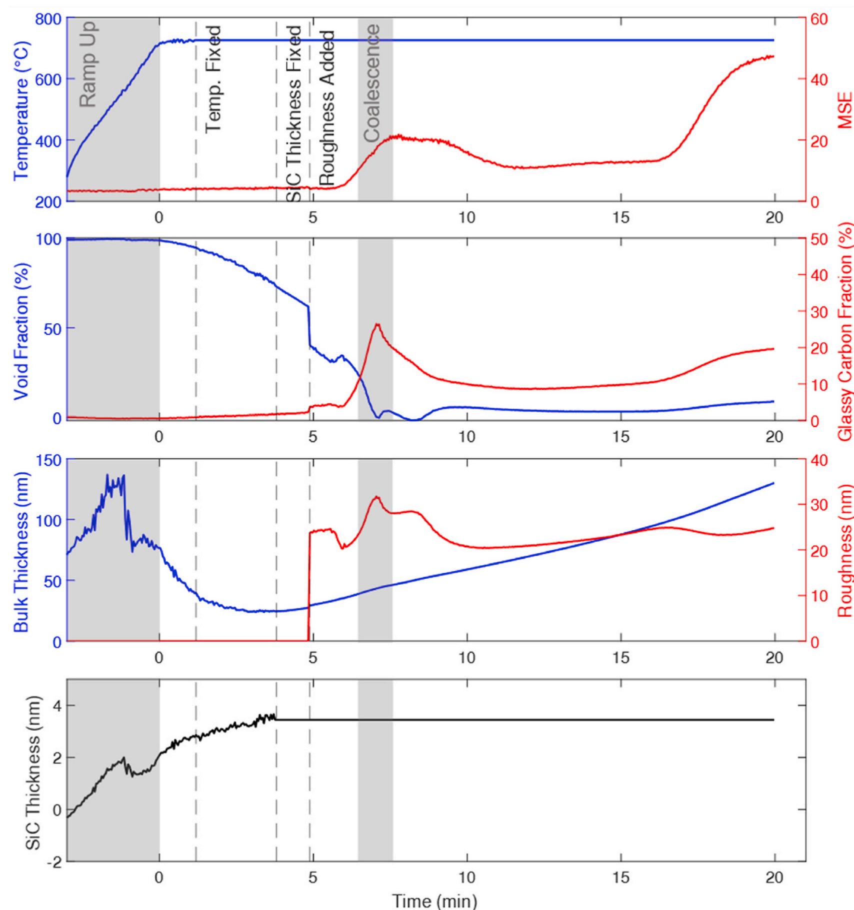

Fig. 8. In-situ SE-measured data from a 20-min growth at 5% methane concentration. From top panel: SE-measured temperature and MSE; bulk layer impurity fractions; bulk thickness and surface roughness; SiC layer thickness. (A colour version of this figure can be viewed online.)

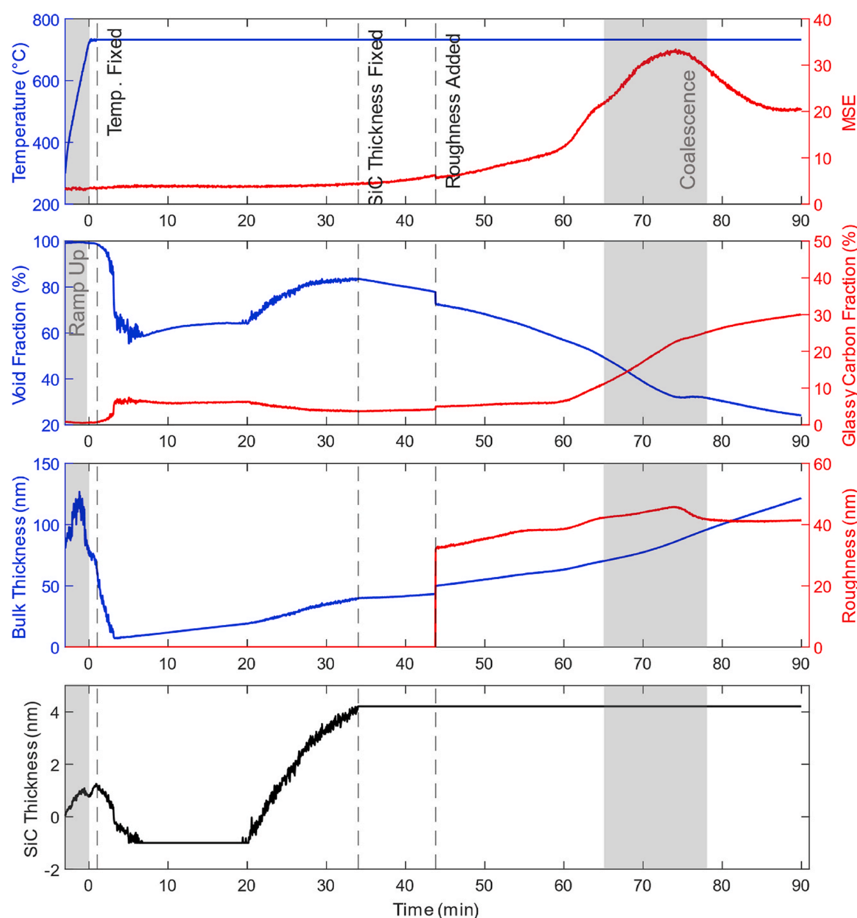

Fig. 9. In-situ SE-measured data from a 90-min growth at 1% methane concentration. From top panel: SE-measured temperature and MSE; bulk layer impurity fractions; bulk thickness and surface roughness; SiC layer thickness. (A colour version of this figure can be viewed online.)

with growth duration, with a coalesced film visible by 30 min of growth. The RMS roughness increases with growth duration, although the rate of increase is greater in the first 15 min of growth. The trend of a peak in RMS roughness at the point of coalescence seen in the *in-situ* spectra and previously observed by Thomas et al. [28] is not seen in the AFM images. This is because the *in-situ* SE data indicates that the spike in roughness is seen at approximately 22–27 min, whilst the closest two AFM images are taken at 20 and 30 min respectively, before the appearance and after the disappearance of the SE-measured roughness peak. The maximum roughness depth peaks at 20 min but decreases after this as the voids between crystallites are filled.

3.5. 5% methane

Fig. 8 shows *in-situ* SE-measured parameters for a sample grown for 20 min at a methane concentration of 5%. As with the 3% methane growth, in the first 2 min of growth the model suggested an unrealistically high bulk thickness and void fraction due to high parameter correlation. The level of correlation decreased after 2 min, resulting in more realistic values being suggested by the model. The SE-measured temperature was also fixed after 1 min of growth to avoid the issue of correlation with this parameter. The thickness of the SiC layer parameter presented an issue not seen in the 3% growth; a high level of correlation between this parameter and the bulk thickness was seen after coalescence. As a result, the SiC thickness was fixed in the model prior to coalescence.

Perhaps the most obvious change with the increase in methane concentration was the point of coalescence; this occurred much earlier at around 7 min compared the almost 25 min seen with 3% methane. Additionally, the peak in glassy carbon content at the point of coalescence was higher with 5% methane (26.5% vs 23.5%). It is important to note at this point that whilst the SE model estimates the glassy carbon content within the bulk layer, these numbers are best used for comparison than as absolute compositional values. This higher glassy carbon fraction is likely the result of greater levels of re-nucleation, which is enhanced by higher methane concentration during growth and leads to more sp^2 bonding [1]. Both of these observations are consistent with what has been previously seen *in-situ* by Hong et al. [8,14].

Following coalescence, the growth rate at higher methane concentration was significantly faster than at 3%. From approximately 16 min onwards, the MSE began to increase as a result of depolarisation caused by the increase in surface roughness from overgrowth of crystallites. This does demonstrate the limitation of SE for the characterisation of thicker, rougher, films, indicating that its most effective use is for characterisation of the early stages of growth.

3.6. 1% methane

Fig. 9 shows *in-situ* SE data from a sample grown for 90 min at 1% methane concentration. The point of coalescence is significantly later than at 3% or 5% methane concentration, with the characteristic increase in glassy carbon content not seen until 60 min. The initial peak in glassy carbon content at around 75 min was of a similar magnitude to that seen in the 3% growth. Unlike the other two growths, an initial increase in void content is seen up to 30 min, and the bulk thickness at the point of coalescence is greater. This is likely the result of etching of the diamond seeds by the plasma, which is known to occur at low methane concentrations and can result in a decrease in nucleation

density [20]. Another difference from the other two growth was seen after coalescence. In this case, the glassy carbon content continued to increase at this point, whereas it decreased following coalescence in the other two growths. A clear increase in the gradient of the bulk thickness is seen at around 70 min due to the switch to columnar growth. The thickness of the SiC layer at the time of fixing seen in the 1% growth is slightly greater than that of the 5% growth, typical of the long incubation period for low-methane growth [17].

4. Conclusions

Spectroscopic ellipsometry was used to investigate the early stages of diamond growth on silicon. An iterative fitting process was used to develop an optical model of the substrate and diamond film using *ex-situ* SE spectra, comprising a bulk EMA with optical constants of diamond, void, and glassy carbon (to approximate sp^2 content) atop a silicon substrate, with a third layer to account for surface roughness. This model was validated using AFM images and Raman spectra of samples of growth durations of 5–30 min. The model was then applied to *in-situ* data, taken during the growth process. A parabolic decrease in void content was seen, with the point of coalescence of the individual crystallites marked by a peak in bulk glassy carbon content and surface roughness. The impact of varying methane concentration on the initial stages of growth was also investigated using SE. An increase in the methane concentration to 5% resulted in earlier coalescence and a higher peak glassy carbon fraction, whereas decreasing the methane fraction to 1% significantly delayed coalescence.

The application of SE to diamond growth presents a powerful tool for *in*-situ monitoring of the critical early stages of growth, with a sub-nanometre resolution and ability to identify changes in the composition of the film. This work also opens the door to using SE to further understand the nucleation and early stages of diamond growth on materials that can be challenging to grow diamond on, such as aluminium nitride and gallium nitride.

CRediT authorship contribution statement

William G.S. Leigh: Conceptualization, Methodology, Formal analysis, Investigation, Writing – original draft, Writing – review & editing, Visualization. **Evan L.H. Thomas:** Conceptualization, Formal analysis, Investigation, Writing – review & editing, Supervision. **Jerome A. Cuenca:** Investigation, Writing – review & editing, Supervision. **Soumen Mandal:** Investigation, Writing – review & editing, Supervision. **Oliver A. Williams:** Resources, Supervision, Project administration, Funding acquisition, Conceptualization, Writing - review & editing.

Data availability statement

Information on the data underpinning the results presented here, including how to access them, can be found in the Cardiff University data catalogue at http://doi.org/10.17035/d.2022.0221979270.

Declaration of competing interest

The authors declare that they have no known competing financial interests or personal relationships that could have appeared to influence the work reported in this paper.

Acknowledgements

This work was supported by funding from the EPSRC under the both the Gan-DaME programme grant (EP/P00945X/1) and Centre for Doctoral Training in Diamond Science and Technology (EP/L015315/1).

References

[1] O.A. Williams, Nanocrystalline diamond, Diam. Relat. Mater. 20 (2011) 621–640, https://doi.org/10.1016/j.diamond.2011.02.015.
[2] A.V. Sumant, O. Auciello, M. Liao, O.A. Williams, MEMS/NEMS based on mono-, nano-, and ultrananocrystalline diamond films, MRS Bull. 39 (2014) 511–516, https://doi.org/10.1557/mrs.2014.98.
[3] J.V. Macpherson, A practical guide to using boron doped diamond in electrochemical research, Phys. Chem. Chem. Phys. 17 (2015) 2935–2949, https://doi.org/10.1039/C4CP04022H.
[4] J.W. Pomeroy, R.B. Simon, H. Sun, D. Francis, F. Faili, D.J. Twitchen, M. Kuball, Contactless thermal boundary resistance measurement of GaN-on-Diamond wafers, IEEE Electron. Device Lett. 35 (2014) 1007–1009, https://doi.org/10.1109/LED.2014.2350075.
[5] M.D. Smith, J.A. Cuenca, D.E. Field, Y. Fu, C. Yuan, F. Massabuau, S. Mandal, J. W. Pomeroy, R.A. Oliver, M.J. Uren, K. Elgaid, O.A. Williams, I. Thayne, M. Kuball, GaN-on-diamond technology platform: bonding-free membrane manufacturing process, AIP Adv. 10 (2020), 035306, https://doi.org/10.1063/1.5129229.
[6] J. Philip, P. Hess, T. Feygelson, J.E. Butler, S. Chattopadhyay, K.H. Chen, L. C. Chen, Elastic, mechanical, and thermal properties of nanocrystalline diamond films, J. Appl. Phys. 93 (2003) 2164–2171, https://doi.org/10.1063/1.1537465.
[7] H. Sun, R.B. Simon, J.W. Pomeroy, D. Francis, F. Faili, D.J. Twitchen, M. Kuball, Reducing GaN-on-diamond interfacial thermal resistance for high power transistor applications, Appl. Phys. Lett. 106 (2015), 111906, https://doi.org/10.1063/1.4913430.
[8] B. Hong, J. Lee, R.W. Collins, Y. Kuang, W. Drawl, R. Messier, T.T. Tsong, Y. E. Strausser, Effects of processing conditions on the growth of nanocrystalline diamond thin films: real time spectroscopic ellipsometry studies, Diam. Relat. Mater. 6 (1997) 55–80, https://doi.org/10.1016/S0925-9635(96)00591-2.
[9] K.A. Snail, C.M. Marks, *In situ* diamond growth rate measurement using emission interferometry, Appl. Phys. Lett. 60 (1992) 3135–3137, https://doi.org/10.1063/1.106747.
[10] C.D. Zuiker, D.M. Gruen, A.R. Krauss, *In situ* laser reflectance interferometry measurement of diamond film growth, J. Appl. Phys. 79 (1996) 3541–3547, https://doi.org/10.1063/1.361406.
[11] S. Saada, S. Pochet, L. Rocha, J.C. Arnault, P. Bergonzo, Real time investigation of diamond nucleation by laser scattering, Diam. Relat. Mater. 18 (2009) 707–712, https://doi.org/10.1016/j.diamond.2009.01.044.
[12] A.C. Ferrari, J. Robertson, Origin of the 1 1 5 0 − cm − 1 Raman mode in nanocrystalline diamond, Phys. Rev. B 63 (2001), 121405, https://doi.org/10.1103/PhysRevB.63.121405.
[13] Y. Cong, R.W. Collins, G.F. Epps, H. Windischmann, Spectroellipsometry characterization of optical quality vapor-deposited diamond thin films, Appl. Phys. Lett. 58 (1991) 819–821, https://doi.org/10.1063/1.104499.
[14] B. Hong, M. Wakagi, R.W. Collins, I. An, N.C. Engdahl, W. Drawl, R. Messier, Real-time spectroscopic ellipsometry studies of diamond film growth by microwave plasma-enhanced chemical vapour deposition, Diam. Relat. Mater. 3 (1994) 431–437, https://doi.org/10.1016/0925-9635(94)90198-8.
[15] H. Fujiwara, Spectroscopic Ellipsometry: Principles and Applications, John Wiley & Sons, Chichester, England ; Hoboken, NJ, 2007.
[16] G. Koster, G. Rijnders (Eds.), In-situ Characterization of Thin Film Growth, Woodhead Publishing, Cambridge ; Philadelphia, PA, 2011.
[17] X. Jiang, K. Schiffmann, C.-P. Klages, Nucleation and initial growth phase of diamond thin films on (100) silicon, Phys. Rev. B 50 (1994) 8402–8410, https://doi.org/10.1103/PhysRevB.50.8402.
[18] S. Mandal, Nucleation of diamond films on heterogeneous substrates: a review, RSC Adv. 11 (2021) 10159–10182, https://doi.org/10.1039/D1RA00397F.
[19] J.J. Gracio, Q.H. Fan, J.C. Madaleno, Diamond growth by chemical vapour deposition, J. Phys. D Appl. Phys. 43 (2010), 374017, https://doi.org/10.1088/0022-3727/43/37/374017.
[20] W.S. Yang, J.H. Je, Effects of secondary pretreatments of substrate on the nucleation of diamond film, J. Mater. Res. 11 (1996) 1787–1794, https://doi.org/10.1557/JMR.1996.0224.
[21] J. Hees, A. Kriele, O.A. Williams, Electrostatic self-assembly of diamond nanoparticles, Chem. Phys. Lett. 509 (2011) 12–15, https://doi.org/10.1016/j.cplett.2011.04.083.
[22] P. Ascarelli, S. Fontana, Dissimilar grit-size dependence of the diamond nucleation density on substrate surface pretreatments, Appl. Surf. Sci. 64 (1993) 307–311, https://doi.org/10.1016/0169-4332(93)90201-L.
[23] Sh Michaelson, O. Ternyak, A. Hoffman, Y. Lifshitz, Correlation between diamond grain size and hydrogen retention in diamond films studied by scanning electron microscopy and secondary ion mass spectroscopy, Appl. Phys. Lett. 90 (2007), 031914, https://doi.org/10.1063/1.2432996.
[24] Ch Wild, N. Herres, P. Koidl, Texture formation in polycrystalline diamond films, J. Appl. Phys. 68 (1990) 973–978, https://doi.org/10.1063/1.346663.
[25] A. van der Drift, Evolutionary selection, a principle governing growth orientation in vapour-deposited layers, Philips Res. Rep. 22 (1967) 267–268.
[26] J. Cifre, J. Campmany, E. Bertran, J. Esteve, Spectroscopic ellipsometry measurements of the diamond-crystalline Si interface in chemically vapour-deposited polycrystalline diamond films, Diam. Relat. Mater. 2 (1993) 728–731, https://doi.org/10.1016/0925-9635(93)90212-K.
[27] N. Cella, H. El Rhaleb, J.P. Roger, D. Fournier, E. Anger, A. Gicquel, Ex-situ spectroscopic ellipsometry studies of micron thick CVD diamond films, Diam. Relat. Mater. 5 (1996) 1424–1432, https://doi.org/10.1016/S0925-9635(96)00578-X.

[28] E.L.H. Thomas, S. Mandal, Ashek-I-Ahmed, J.E. Macdonald, T.G. Dane, J. Rawle, C.-L. Cheng, O.A. Williams, Spectroscopic ellipsometry of nanocrystalline diamond film growth, ACS Omega 2 (2017) 6715–6727, https://doi.org/10.1021/acsomega.7b00866.
[29] W. Kern, D.A. Puotinen, Cleaning solutions based on hydrogen peroxide for use in silicon semiconductor technology, RCA Rev. 31 (1970) 187–206.
[30] W. Kern, The evolution of silicon wafer cleaning technology, J. Electrochem. Soc. 137 (1990) 1887, https://doi.org/10.1149/1.2086825.
[31] S.M. Leeds, T.J. Davis, P.W. May, C.D.O. Pickard, M.N.R. Ashfold, Use of different excitation wavelengths for the analysis of CVD diamond by laser Raman spectroscopy, Diam. Relat. Mater. 7 (1998) 233–237, https://doi.org/10.1016/S0925-9635(97)00261-6.
[32] E.D. Palik, Handbook of Optical Constants of Solids, Nachdr., Acad. Press, San Diego, Calif., 2003.
[33] C.M. Herzinger, B. Johs, W.A. McGahan, J.A. Woollam, W. Paulson, Ellipsometric determination of optical constants for silicon and thermally grown silicon dioxide via a multi-sample, multi-wavelength, multi-angle investigation, J. Appl. Phys. 83 (1998) 3323–3336, https://doi.org/10.1063/1.367101.
[34] M.W. Williams, E.T. Arakawa, Optical properties of glassy carbon from 0 to 82 eV, J. Appl. Phys. 43 (1972) 3460–3463, https://doi.org/10.1063/1.1661738.
[35] D.N. Belton, S.J. Harris, S.J. Schmieg, A.M. Weiner, T.A. Perry, *In situ* characterization of diamond nucleation and growth, Appl. Phys. Lett. 54 (1989) 416–417, https://doi.org/10.1063/1.100938.
[36] M. Ishii, K. Nakashima, I. Tajima, M. Yamamoto, Properties of silicon surface cleaned by hydrogen plasma, Appl. Phys. Lett. 58 (1991) 1378–1380, https://doi.org/10.1063/1.105211.
[37] J.C. Arnault, S. Saada, M. Nesladek, O.A. Williams, K. Haenen, P. Bergonzo, E. Osawa, Diamond nanoseeding on silicon: stability under H2 MPCVD exposures and early stages of growth, Diam. Relat. Mater. 17 (2008) 1143–1149, https://doi.org/10.1016/j.diamond.2008.01.008.
[38] B.R. Stoner, G.-H.M. Ma, S.D. Wolter, J.T. Glass, Characterization of bias-enhanced nucleation of diamond on silicon by invacuo surface analysis and transmission electron microscopy, Phys. Rev. B 45 (1992) 11067–11084, https://doi.org/10.1103/PhysRevB.45.11067.
[39] B.D. Johs, C.M. Herzinger, Methods for uncorrelated evaluation of parameters in parameterized mathematical model equations for window retardence, in: Ellipsometer and Polarimeter Systems, US6034777A, 2000. https://patents.google.com/patent/US6034777/en. (Accessed 11 July 2022).
[40] O.A. Williams, M. Daenen, J. D'Haen, K. Haenen, J. Maes, V.V. Moshchalkov, M. Nesládek, D.M. Gruen, Comparison of the growth and properties of ultrananocrystalline diamond and nanocrystalline diamond, Diam. Relat. Mater. 15 (2006) 654–658, https://doi.org/10.1016/j.diamond.2005.12.009.
[41] O.A. Williams, A. Kriele, J. Hees, M. Wolfer, W. Müller-Sebert, C.E. Nebel, High Young's modulus in ultra thin nanocrystalline diamond, Chem. Phys. Lett. 495 (2010) 84–89, https://doi.org/10.1016/j.cplett.2010.06.054.
[42] Z.G. Hu, P. Hess, Optical constants and thermo-optic coefficients of nanocrystalline diamond films at 30–500°C, Appl. Phys. Lett. 89 (2006), 081906, https://doi.org/10.1063/1.2243863.
[43] H.G. Tompkins, A User's Guide to Ellipsometry, Elsevier Science, Saint Louis, 2014.
[44] P.G. Snyder, J.A. Woollam, S.A. Alterovitz, B. Johs, Modeling AlxGa1−xAs optical constants as functions of composition, J. Appl. Phys. 68 (1990) 5925–5926, https://doi.org/10.1063/1.346921.
[45] J. Woollam, B. Johs, C. Herzinger, J. Hilfiker, R. Synowicki, C. Bungay, Overview of variable angle spectroscopic ellipsometry (VASE), Part I: basic theory and typical applications, Proc. SPIE-Int. Soc. Opt. Eng. 1 (1999) 3–28.
[46] I. Villalpando, P. John, S. Porro, J.I.B. Wilson, Hydrogen plasma etching of diamond films deposited on graphite, Diam. Relat. Mater. 20 (2011) 711–716, https://doi.org/10.1016/j.diamond.2011.03.007.
[47] P.B. Barna, M. Adamik, Fundamental structure forming phenomena of polycrystalline films and the structure zone models, Thin Solid Films 317 (1998) 27–33, https://doi.org/10.1016/S0040-6090(97)00503-8.
[48] J.H. Parker, D.W. Feldman, M. Ashkin, Raman scattering by silicon and germanium, Phys. Rev. 155 (1967) 712–714, https://doi.org/10.1103/PhysRev.155.712.
[49] C.S. Wang, J.M. Chen, R. Becker, A. Zdetsis, Second order Raman spectrum and phonon density of states of silicon, Phys. Lett. 44 (1973) 517–518, https://doi.org/10.1016/0375-9601(73)91001-3.
[50] S. Tóth, P. Németh, P. Rácz, L. Himics, P. Dombi, M. Koós, Silicon carbide nanocrystals produced by femtosecond laser pulses, Diam. Relat. Mater. 81 (2018) 96–102, https://doi.org/10.1016/j.diamond.2017.11.014.
[51] F. Cerdeira, T.A. Fjeldly, M. Cardona, Raman study of the interaction between localized vibrations and electronic excitations in boron-doped silicon, Phys. Rev. B 9 (1974) 4344–4350, https://doi.org/10.1103/PhysRevB.9.4344.
[52] M. Chandrasekhar, H.R. Chandrasekhar, M. Grimsditch, M. Cardona, Study of the localized vibrations of boron in heavily doped Si, Phys. Rev. B 22 (1980) 4825–4833, https://doi.org/10.1103/PhysRevB.22.4825.
[53] A.C. Ferrari, J. Robertson, A.C. Ferrari, J. Robertson, Raman spectroscopy of amorphous, nanostructured, diamond–like carbon, and nanodiamond, Philos. Trans. R. Soc. London, Ser. A: Math. Phys. Eng. Sci. 362 (2004) 2477–2512, https://doi.org/10.1098/rsta.2004.1452.
[54] J.A. Cuenca, E. Thomas, S. Mandal, O. Williams, A. Porch, Microwave determination of sp2 carbon fraction in nanodiamond powders, Carbon 81 (2015) 174–178, https://doi.org/10.1016/j.carbon.2014.09.046.
[55] A.C. Ferrari, Raman spectroscopy of graphene and graphite: disorder, electron–phonon coupling, doping and nonadiabatic effects, Solid State Commun. 143 (2007) 47–57, https://doi.org/10.1016/j.ssc.2007.03.052.